Light-activated helical inversion in cholesteric liquid crystal microdroplets

Piotr Sleczkowski[a,b,1], Ye Zhou[c,1], Supitchaya Iamsaard[a], Juan J. de Pablo[c,2], Nathalie Katsonis[a,2], and Emmanuelle Lacaze[b,2]

[a]Bio-inspired and Smart Materials, MESA+ Institute for Nanotechnology, University of Twente, 7500 AE Enschede, The Netherlands; [b]Sorbonne Universités, CNRS, Institut des NanoSciences de Paris (INSP), F-75005 Paris, France; and [c]Institute for Molecular Engineering, The University of Chicago, Chicago, IL 60637

Cholesteric liquid crystal (CLC) droplets exhibit nontrivial topological features, which are controlled by the ratio between the cholesteric pitch and the droplet radius. The radial spherical structure (RSS) is of particular interest, as it reveals an onion-like concentric organization of the cholesteric helices, leading to the expression of spherical Bragg microcavities. Using an overcrowded alkene-based unidirectional molecular motor as a dopant, we show that the topological defect structure in the droplet can be activated by illumination. By using appropriate molecular motor concentrations, light can either break the symmetry of topological defects (as observed for the bent-twisted bipolar structure), or it can induce inversion of handedness in an onion-like organization (in the case of RSS). This latter feature may pave the way toward alternative activation modes of lasers based on cholesteric droplets. By also studying CLC droplets once they have reached full photoconversion at photostationary state (PSS), we highlight that the strong influence of confinement on the droplets structure occurs to the same extent after the helix inversion event. Our results are interpreted in terms of numerical simulations of the droplets' structure, which shed light on the major role played by curvature close to the droplets' center, this latter one becoming dominant when the droplet radius is small.

chiral liquid crystals | droplets | confinement | photoinduced helix inversion | molecular motors

The emerging area of soft photonics has attracted considerable interest over the last decade (1–5). Thermotropic liquid crystals (LCs) have played an important role in that field. In chiral nematic (cholesteric) liquid crystals (CLCs), the helical structure induces a one-dimensional photonic bandgap that is centered at the wavelength $\lambda_0 = np_i$, where n and p_i stand for the average refractive index and the cholesteric pitch, respectively. The helical organization is further manifested by the selective reflection of circularly polarized light of the same handedness as the cholesteric helix. Recently, liquid crystals in complex geometries have attracted attention, in particular droplets (6) and shells (7), with a special emphasis on studies of topological defects (8), the tunability of the systems (9, 10), and a combination of both (11). For example, Humar and Mušević (12) have shown that CLC microdroplets can act as spherical Bragg onion microcavities, presenting the first omnidirectional microlaser. Tuning of the emission wavelength was perfomed by adjusting temperature, since the cholesteric pitch is temperature-sensitive (13). Such demonstrations have served to establish that CLC droplets should be considered as components for different types of optical microcavities, with potential applications in (bio)sensing (14–16), optical telecommunications, and displays (17). As a next step, it would be interesting to tune not only the CLC period, but also the CLC pitch handedness. The possibility of reversible tuning between left- and right-handed CLC droplets of controlled shape and size is a challenging goal that would open up new opportunities for development of circularly polarized light-responsive materials and devices (18–21).

The main advantage of using LCs as a gain medium comes from the possibility of tuning spectral properties by manipulating an applied electric field (10) or the temperature (12). For photoresponsive LCs, light can be viewed as an alternative stimulus that, compared with heat or voltage, offers the advantage of ease of addressability, fast response time, and potential remote control (22). A photoresponsive CLC may be prepared by doping an achiral nematic LC host with a few wt % of a photosensitive chiral molecular switch or motor, which will induce a twist and a helical structure in the mesophase, and will act as a trigger when irradiated with light of a proper wavelength (23). If the helical twisting power (HTP) of the irradiated motor is sufficiently large and of different sign (with respect to that of the nonirradiated material), an inversion of the handedness could be achieved in the photostationary state (PSS). Past reports on photoinduced handedness inversion in CLCs doped with photoresponsive chiral dopants have been largely limited to chiral azobenzenes (24), chiral diarylethenes (25), and overcrowded alkenes (26, 27). Among these, overcrowded alkene-based unidirectional molecular motors are proven to be the most efficient photoswitchable dopants for LCs (28). Upon irradiation, CLC films doped with molecular motors undergo a reorganization related to the modification of HTP, induced by the evolution of dopant molecules, which is manifested by the rotation of the surface texture (29). In this work, we ask how irradiation will modify the texture of CLC droplets, and how handedness inversion might proceed in such droplets. The long-term goal would be to use droplets in future applications for manipulation of optical properties. To

Significance

Controlled switching between right- and left-handedness in spherical cholesteric droplets could lead to easily manufacturable objects for diverse applications in optoelectronics, especially in the area of circularly polarized light-responsive materials and devices. In this work, we show that photoinduced inversion of the cholesteric helix is supported in spherical droplets of a nematic liquid crystal doped with a chiral light-driven molecular motor. We show how the handedness inversion occurs in the sequence of phase transitions induced by light irradiation, combining experiments on several hundreds of droplets and simulations. We demonstrate the strong influence of the confinement on the droplet structure and on the dynamics under light irradiation, which allows for this handedness inversion.
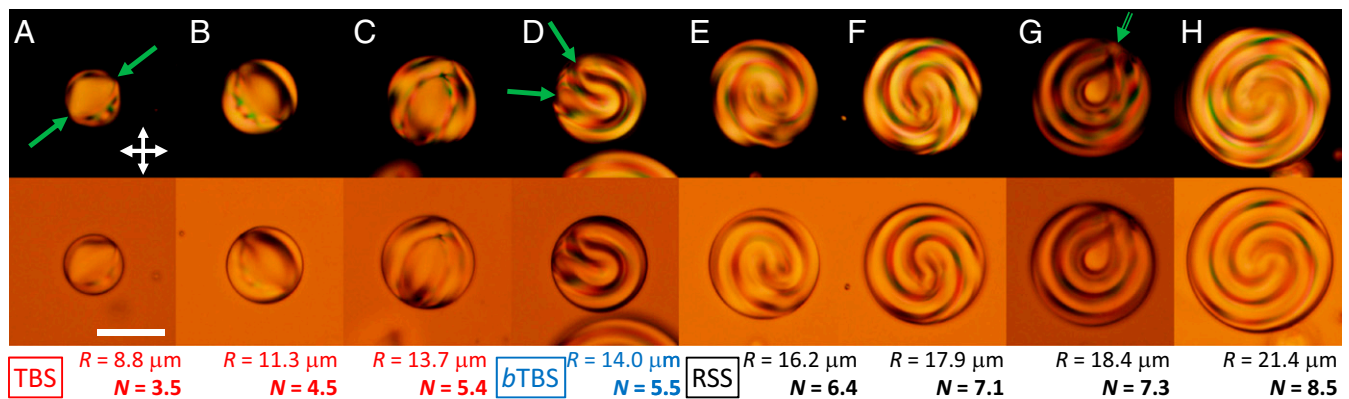
Fig. 1. Structural diversity of the cholesteric droplets of **1a** CLC mixture with $p_{i(1a)} = 10.12$ μm, under crossed polarizers and with no analyzer configuration. Transition from TBS to RSS may be noticed for the increasing radius of droplet. *A–C* show droplets in TBS, *D* shows droplet in *b*TBS, and *E–H* show droplets in RSS. Green arrows on *A*, *D*, and *G* indicate orientation of surface defects for TBS, *b*TBS, and RSS, respectively. Crossed arrows represent orientation of a polarizer–analyzer pair. (Scale bar: 20 μm.)

obtain a comprehensive view of CLC droplets behavior, we use a dispersion technique for the fabrication of CLC droplets, allowing us to obtain a wide range of droplet sizes. However, we presume that the output would be similar if another method of fabrication (e.g., microfluidic) is used, in particular for the preparation of monodisperse droplets.

Previous theoretical (30–32) and experimental (33, 34) studies of CLC droplets revealed the existence of two main director configurations, whose stability depends on the R/p_i ratio, where R is the radius of the droplet and p_i the intrinsic pitch. Xu and Crooker (34) showed that for $p_i > R$, CLC droplets adopt a so-called twisted bipolar structure (TBS), characterized by two diametrically opposite surface defects (boojums). Thus, the associated director field exhibits a cylindrical symmetry, with the symmetry axis consisting of a λ^{+1} disclination line joining both boojums. When $p_i < R$, the director field takes on a radial spherical structure (RSS), characterized by an onion-like texture associated with a radial defect originating from the center of the droplet and pointing to its surface. In addition, an intermediate state between the TBS and RSS states, the so-called bent-TBS (*b*TBS), has been theoretically and experimentally identified. In that state, the nonantipodal orientation of two surface defects reflects a broken cylindrical symmetry (35).

Past reports on photoinduced changes in spherical CLC droplets concentrated on ordering transitions at the surface of the droplet (36), with optical (on/off) switching of CLC droplets (20), or with manipulation of the topological states of CLC droplets (37). The studies of cholesteric helix inversion are not numerous and most often limited to CLC films (38) and sessile droplets deposited on a substrate (39). Unlike the temperature-

driven helix inversion in CLC droplets (33), the photoinduced helix inversion in spherical CLC droplets was reported very recently with the demonstration that cholesteric unwinding followed by another winding could occur in cholesteric droplets under light irradiation in the presence of a mixture of molecular dopants (40).

In this paper, we investigate the process of photoinduced helix inversion in spherical CLC droplets combining a theoretical and experimental study using a single dopant only. We show that all droplet structures (from RSS to *b*TBS and TBS) are formed during UV irradiation, until a pseudonematic state is reached and the inversion of handedness of the droplet is achieved. For clarity, we introduce a parameter relating droplet size and cholesteric pitch, $N = 4R/p_i$, which stands for the number of π-turns of a nonconfined helix along the diametrical axis of the droplet. We show that, depending on the initial value of N, either a TBS structure is reached at the PSS state, or a *b*TBS of reverse symmetry, or an RSS state of reverse handedness if the initial N value was sufficiently large. By relying on simulations of droplets' structure, we analyze in detail the role of confinement on the droplet structure and the dynamics under light irradiation.

Results

Static Analysis of CLC Droplets. In a first step, it is important to understand the behavior of the droplets as a function of their size before irradiation. The first set of experiments is thus devoted to a static description of the structural characteristics of CLC droplets in glycerol. CLCs were prepared by doping the commonly used eutectic liquid crystal mixture E7 with the photosensible molecular
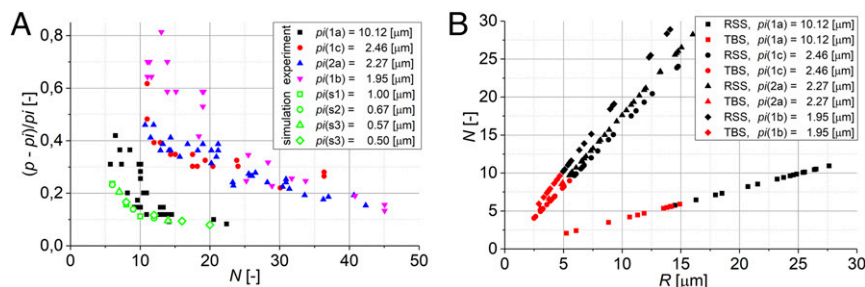

Fig. 2. Summary of the structural diversity in the CLC droplets. (*A*) The relative change of the period, *p*, to the intrinsic cholesteric pitch, p_i, as a function of the respective geometrical confinement, *N* for the four experimental p_i values (in bold) and four simulated p_i values (hollow green symbols). (*B*) Phase diagram depicting the transition between the RSS (black symbols) and TBS (red symbols) for the as-prepared CLC droplets. The diminishing of the *N* value at which the structural transition occurs as the intrinsic cholesteric pitch is increased is noticeable.
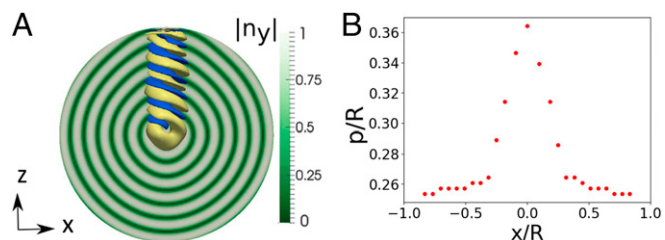
Fig. 3. Results of simulations of cholesteric droplets. (*A*) The *x*–*z* cross-section of a CLC droplet for $R = 2$ μm and $N = 16$. The director field is colored according to its projection on the *y* axis. The splay and bend distortions are shown in blue ($S_{SB} > 0.0014$) and yellow ($S_{SB} < -0.0014$), respectively. (*B*) The evolution of period *p*, estimated by maxima and minima of directors' *y* component along the diametrical direction in the *x* axis. The value of $p_i/R = 4/N = 0.25$.

motor 9-(2-Methyl-2,3-dihydro-1H-cyclopenta[a]naphthalen-1-ylidene)-9H-fluorene (Fig. S1 *A and B*; see *Experimental* for preparation details). We prepared four different CLC mixtures with various concentrations of the motor molecule, leading to four different values of the cholesteric pitch, noted p_i, measured in wedge cells according to the known value of the HTP for the motor/E7 system (Fig. S1*C*, HTP = 43.33 μm^{-1}) (41). The resulting dispersions contained hundreds of droplets with planar anchoring, which were analyzed with the use of a polarized optical microscope (POM) according to their size and texture. In Fig. 1, a set of droplets of CLC mixture **1a** (cholesteric pitch $p_{i(1a)} = 10.12$ μm) is presented under crossed polarizers, for increasing radius, *R*, and thus leading to increasing *N*, in the range between 3.5 and 8.5. Fig. 1*A* shows a droplet with $N = 3.5$, which reveals a typical TBS texture with two antipodal defects highlighted by green arrows. This result is in agreement with previous experimental studies (34), and theoretical investigations of Seč et al. (32), who found that TBS is the most stable configuration for $N < 4$ (i.e., $p_i > 4R$). However, the same studies concluded that for $N > 4$ the most stable structure is RSS, which is not the case for the system presented in Fig. 1. Neither for $N = 4.5$ nor for $N = 5.4$ (Fig. 1 *B* and *C*) is it possible to identify any features associated with RSS. The first clear signs of losing the symmetric character of the TBS texture are seen for a droplet with $N = 5.5$ (Fig. 1*D*). Further analysis of the system shows that as soon as *N* exceeds 6.4, no structure other than RSS is observed. RSS is manifested by the texture containing either a spiraling or an onion-like feature, respectively, depending on whether or not the radial defect is oriented perpendicularly to the plane of view (Fig. 1 *E*, *F*, and *H* compared with Fig. 1*G*). The surface point of the double-helix radial defect is highlighted by the green arrow in Fig. 1*G*. Overall, we find two regimes of stable TBS and RSS structures, separated by an intermediate regime, spanning between $N \sim 5.5$ and $N \sim 6.4$. This intermediate regime, referred to as bent-TBS, is characterized by two nonantipodal defects, i.e., the two radii containing the surface defects form an angle between 50° and 180° (35, 42).

Fig. 2 summarizes the structural diversity of the as-prepared CLC droplets. We first analyze the RSS droplets, and the spiraling/onion-like feature. In Fig. 2*A* we examine the evolution of the onion period *p*, defined as the distance between every second feature. More precisely, the relative change of the period (*p*) to the cholesteric pitch (p_i), defined as $(p - p_i)/p_i$, is shown as a function of geometrical confinement for each droplet, *N*. Obviously for all four mixtures considered here, the period drastically increases with decreasing *N*, i.e., with increasing confinement. It should be noted that the relative change of the period for the **1a** mixture (black squares, Fig. 2*A*) reaches a maximum value 0.4 (for $N = 6$ and $p_{i(1a)} = 10.12$ μm), while for the high-chirality mixtures (magenta triangles, Fig. 2*A*) it reaches values in the range between 0.7 and 0.8 (for $N = 11$ and $p_{i(1c)} = 1.95$ μm). Also note that even for the largest of the droplets examined here (**1a**: $N \sim 20$, **1b/1c/2a**: $N \sim 45$), the discrepancy between the period and the respective cholesteric pitch remains around 0.1. A phase diagram of the

RSS–TBS transitions (Fig. 2*B*) was constructed by analyzing hundreds of droplets of four CLC mixtures, with black and red symbols representing RSS and TBS droplets, respectively. One can see that the higher the chirality of the mixture [i.e., the lower the p_i and virtually: the steeper the $N(R)$ slope], the higher the value of the transition parameter, N_{trans}, which varies between 6 and 10 when p_i varies between 10.12 and 1.95 μm. This trend is in agreement with previous experimental results (34).

To understand this experimental behavior, we carried out simulations of CLC droplets with planar anchoring, using a Landau–de Gennes model and a tensorial description of the local order. Fig. 3*A* and Fig. S2 show the periodic variation of the *y*-component director along the diametric direction of an RSS droplet ($R = 2$ μm, $N = 16$). According to the definition of the period (*p*), the distance between every other peak is a measure of p_i under spherical confinement. As shown in Fig. 3*B*, there is a significant change of period near the center of the droplet in comparison with values obtained closer to the droplets surface. In particular, for a droplet characterized by $p_i/R = 0.25$, the spherical confinement results in p/R equal to 0.36 and 0.253 for $|x/R| \sim$ 0.0 and $|x/R| \sim 1.0$, respectively, *x* being the *x* coordinate with the droplet center as origin. As illustrated by the splay-bend–order isosurfaces in Fig. 3*A*, the twisting features near the CLC droplet center suffer from a considerable amount of bend elastic distortion. As a result, the twisting features near the droplet center expand due to a delicate interplay between the elasticity, chirality, and anchoring, leading to a local increase of the period near the center of the droplet and thus an increase of the average period, *p*.

This feature leads to a variation of *p* when *N* varies, which is shown in the comparison between experimental and simulated results in Fig. 2*A* (full vs. hollow green symbols, respectively). As *N* increases, the larger value of $(p - p_i)/p_i$ near the droplet center is averaged out by an increasing number of twisting layers. As a consequence (and the same is true for the experimental results), $(p - p_i)/p_i$ decreases when *N* increases, leading to good agreement between experimental and simulated variations of *p* with *R* (Fig. 2*A*). However, throughout our simulations, we could not reach a value of $(p - p_i)/p_i$ as high as 0.7, which was observed in our experiments for the smallest p_i values (from 1.95 to 2.46 μm). In
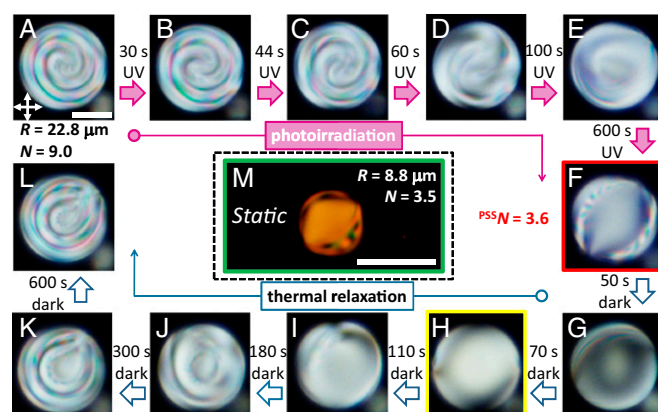

Fig. 4. Optical control of chirality in a cholesteric droplet of **1a** CLC mixture (low-chirality case). A sequence of images showing the photoinduced evolution from RSS to TBS structure, with the gradual increase of the observed period and the rotation of texture (*A–E*), followed by the appearance of the diagonally oriented defects characteristic to TBS (*F*). After turning off the UV irradiation, the relaxation process commenced by the vanishing of the meridian lines (*G*) and the subsequent formation of the pseudonematic state (*H*). Then, the reorientation of defects occurred (*I*), and the droplet started to re-form the spiraling feature (*J*) and restored the RSS (*K*) with the period similar to the initial value (*L*). However a different orientation of the radial defect was revealed (*L*). (*M*) shows a TBS droplet of **1a** mixture of $N = 3.5$, the value of which is close to *N* of photoirradiated droplet at PSS, $^{PSS}N = 3.6$. Crossed arrows represent orientation of a polarizer–analyzer pair. (Scale bar: 20 μm.)
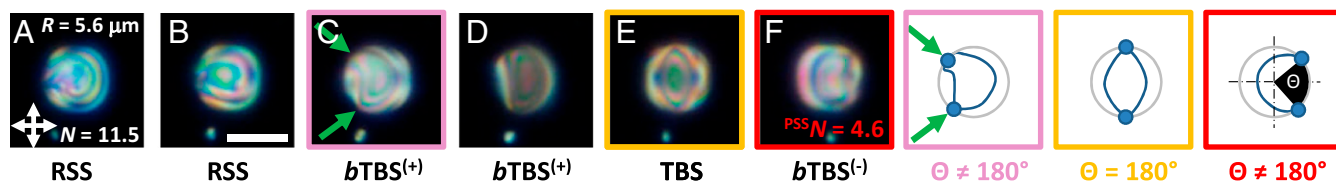
Fig. 5. Evidencing the helix inversion for droplet of **1b** CLC mixture (high-chirality case). (*A*) Droplet before the illumination, $R = 5.6$ μm, $N = 11.5$. Sequence of images taken after illumination time: (*B*) 44, (*C*) 60, (*D*) 66, (*E*) 150, and (*F*) 300 s (PSS with $^{PSS}N = 4.6$). The violet, orange, and red schemes underline the position of defects from the respective frames (*C*), (*E*), and (*F*). The green arrows in *C* and violet frame indicate the defects position. Crossed arrows represent orientation of a polarizer–analyzer pair. (Scale bar: 10 μm.)

agreement with past results (32, 35), we also observed a structural transition of our droplets ($R = 0.5, 0.75$, and 1 μm for a pitch varying between 0.5 and 1.33 μm) from the TBS to the RSS configuration.

Dynamic Analysis of CLC Droplets. The study of the photoresponse of the CLC droplets doped with the molecular motor was carried out in the presence of a constant UV irradiation ($\lambda = 365$ nm, nominal intensity of 1 mW cm^{-2} at 2.5 cm, duration 10 min) until the PSS was reached, with the $^{PSS}HTP = -17.33$ μm^{-1}, as measured in a Grandjean Cano wedge cell (41). The relaxation (after turning off the UV lamp) was then studied in subsequent experiments.

Fig. 4 shows a typical sequence of light-induced structural changes for a low-chirality CLC mixture ($p_{i(1a)} = 10.12$ μm) droplet of radius $R = 22.8$ μm and $N = 9.0$. Clear changes of the CLC texture are observed in response to the photoisomerization of the molecular motor. As the ratio between the photoinduced left-handed photoisomer and the right-handed initial form of the dopant increases, the resulting HTP of the CLC decreases and the RSS period, p, increases (Fig. 4 *A–C*). A counterclockwise rotation of the spiraling feature is simultaneously observed, over up to 60 s of irradiation (Fig. 4*D*), after which it disappears. Then, an intermediate phase associated with the appearance of two surface defects (situated at around 2 o'clock and 7 o'clock, Fig. 4*E*) reveals the *b*TBS structure, which undergoes a rotation until it finally forms a TBS, with the two antipodal boojums (at around 1 o'clock and 7 o'clock, Fig. 4*F*). No further structural changes are observed, evidencing that the PSS is attained, for which the HTP of the motor/E7 mixture corresponds to $^{PSS}N = 3.6$. This value is in agreement with a static TBS texture for the same N value, as shown by the comparison between Fig. 4 *F* and *M*. Right after the UV illumination is turned off, the relaxation process starts with the two diametrically oriented defects continuously moving clockwise, through 2 o'clock/8 o'clock (Fig. 4*G*), and 3 o'clock/9 o'clock (Fig. 4*H*) to 6 o'clock/12 o'clock (Fig. 4*I*) positions, respectively. In the following phase, the intermediate state is not so clear, due to the defects' orientations, but an onion shape appears after 180 s, corresponding to the reverse transition to RSS (Fig. 4*K*). Finally, the original period of the droplet is restored (Fig. 4*L*); however, the radial defect appears reoriented with respect to its original position, which also did not allow for a proper determination of the rotation of the spiraling feature. Note that irradiation was too fast to clearly identify the turning point between two chirality signs that should occur between Fig. 4 *E* and *F*; however, during the relaxation process a pseudonematic texture, associated with a compensated nematic phase and an infinite helix, was clearly observed (Fig. 4*H*). This demonstrates the successful change of chirality handedness between the PSS state and the final relaxed state, or between the initial RSS droplet and the TBS droplet at the PSS.

Helix inversion appeared more clearly in high-chirality mixtures, as, e.g., the CLC mixture $p_{i(1b)} = 1.95$ μm in a droplet of radius $R = 5.6$ μm and $N = 11.5$, which during the irradiation transforms from RSS to an eventual PSS that is not a TBS state, but a *b*TBS, in agreement with the expected value $^{PSS}N = 4.6$ (Fig. 5 where only the irradiation process is shown). At first, it transforms from RSS (Fig. 5*A*) into *b*TBS (Fig. 5*C*), where the two defects are highlighted by green arrows (also see the violet frame, Fig. 5). The two defects continue to move apart until the formation

of TBS state (Fig. 5*E*). In contrast to Fig. 4, we observe a breaking of the cylindrical symmetry of TBS, during irradiation, both before (Fig. 5 *C* and *D*) and after the pseudonematic state (Fig. 5*F*), in relation with the formation of *b*TBS, the intermediate between TBS and RSS states. The comparison of the positions of the defects in Fig. 5 *C*, *E*, and *F* (violet, orange, and red frames, respectively) reveals a mirror symmetry between Fig. 5 *C* and *F*, thus evidencing the helix inversion. Although still without the reappearance of the RSS in the PSS, a *b*TBS state is reached here, and it is a step further related to the inversion of the handedness of the cholesteric helix, with respect to the droplet of Fig. 4. It is in agreement with a larger ^{PSS}N (4.6 for Fig. 5*F* vs. 3.6 for Fig. 4*F*), and it is a good demonstration of the quantitative description of the *b*TBS provided by introducing an angle Θ between the two radii containing the surface defects (Fig. 5*F* and the red frame).

Finally, to clearly outline the helix inversion by the (re)forming of the RSS, it is necessary to examine droplets having a relatively large N value. We have chosen droplets of the high-chirality **1b** CLC mixture. An example ($R = 13.0$ μm, $N = 26.6$) is presented in Fig. 6, where again we only show the irradiation part. After completion of the initial stages of the unwinding of the spiraling feature (Fig. 6*B*), the *b*TBS defects separate, with one surface defect moving clockwise, from ~11 o'clock position to 1 o'clock position, as shown in Fig. 6 *C–F*. The two surface defects are clearly observed in a diametric orientation in Fig. 6*F*; they are associated with the TBS formation. In addition, a half-ring appears on the left-hand side of the circumferential region of the
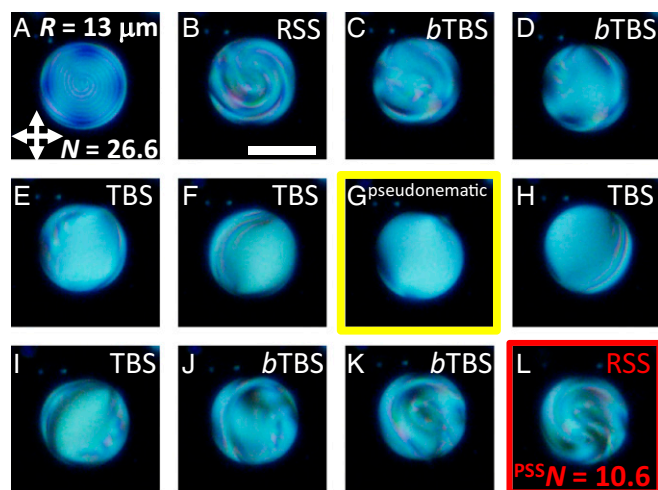

Fig. 6. Evidence of the photoinduced helix inversion in the cholesteric droplet of **1b** CLC mixture (high-chirality case, $p_{i(1b)} = 1.95$ μm). (*A*) Droplet in its initial state, before the illumination is started, $R = 13.0$ μm, $N = 26.6$. Sequence of images taken after illumination time: (*B*) 84, (*C*) 94, (*D*) 98, (*E*) 102, (*F*) 118, (*G*) 126, (*H*) 130, (*I*) 150, (*J*) 190, (*K*) 200, and (*L*) 600 s. The confinement parameter N for the droplet in the PSS, reached after 600 s of irradiation, is equal to $^{PSS}N = 10.6$. Crossed arrows represent orientation of a polarizer–analyzer pair. (Scale bar: 20 μm.)
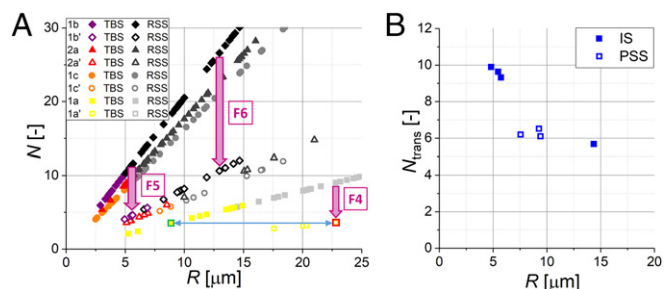
Fig. 7. Phase stability of cholesteric droplets. (*A*) An RSS-TBS phase diagram of the CLC droplets including the droplets in the PSS state. Schematical representation of the photoinduced change of droplets from Figs. 4–6 is depicted by three vertical magenta arrows (F4, F5, and F6). Droplets in the IS and in the PSS are represented by full and hollow symbols, respectively. The blue arrow highlights the comparison between textures from Fig. 4 *F* and *M*. (*B*) A phase stability diagram constructed by averaging the (*N*, *R*) parameters for smallest RSS and largest TBS droplets of each CLC mixture. Full squares represent data in IS, and hollow squares represent PSS. The photoirradiated data for **1a'** mixture are omitted for clarity.

droplet. As a result of further irradiation, this notable feature of the texture is lost (Fig. 6*G*) and almost instantaneously recovered (Fig. 6*H*), with the half-ring present at the right-hand–side hemisphere—evidencing the inversion of handedness. Fig. 6*G* is a perfect illustration of the pseudonematic state, when the net chirality equals zero. After Fig. 6*H*, the cylindrical symmetry is broken in relation to the formation of *b*TBS, with the two surface defects moving toward each other on the right-hand–side part of the circumference (Fig. 6 *I* and *J*). The joining of these two boojums results in the appearance of the spiraling feature— a fingerprint of RSS, shown in Fig. 6*K*. Expressing the chirality in the PSS state by the appearance of the RSS texture (Fig. 6*L*) is permitted due to the sufficiently high value of the confinement parameter, $^{PSS}N = 10.6$.

Discussion

The results shown above demonstrate that we succeeded in inverting the handedness of CLC droplets through the photo-isomerization of an overcrowded alkene-based molecular motor, the handedness inversion being evidenced by clear symmetry changes in the irradiated droplets. The helix inversion of our system not only leads to the reappearance of an RSS texture of inverse handedness, but also to a change of orientation of the *b*TBS state. At the same time, photoirradiation allows one to span the palette of CLC droplet textures by modulating *N*, through the photocontrol of the cholesteric pitch. All of the known structures of CLC droplets (TBS, *b*TBS, and RSS) were obtained both experimentally and in simulations, either by static variations of *N* at a given pitch value, or by dynamical variation of the cholesteric pitch for a given droplet radius. The actual dynamics as revealed in simulations can be viewed in Movie S1. These results suggest that the previous demonstration of a photoisomerization process being slower than the liquid crystal film equilibration under pitch variation, obtained for semifree CLC films (43), still holds for CLC droplets.

As a result, one can use the PSS states to further analyze the phase transition for the study of confinement-induced features in cholesteric droplets. The analysis of Figs. 4–6 shows that the observed RSS states are consistent with the expected structures, i.e., structures based on calculations of ^{PSS}N values for known ^{PSS} HTP. Fig. 7*A* shows an *N* vs. *R* plot that combines the droplets in the initial state with the droplets at PSS, for the four CLC mixtures considered here. Black-grayish and colored symbols represent droplets of RSS and TBS, respectively. Three magenta arrows (F4, F5, and F6) show the photoinduced changes from the initial state (IS) to the PSS for the droplets depicted in Figs. 4, 5, and 6, respectively. The trend observed previously (Fig. 2*B*)

is confirmed in Fig. 7*A*, where additional data from droplets at PSS are included. These results allow us to reproduce the trend of N_{trans} for several values of cholesteric pitch as a function of the droplet radius, N_{trans} being the transition value between TBS and RSS structures. It is defined as an arithmetic average between the size of the largest TBS droplet and the smallest RSS droplet for each cholesteric pitch. The RSS–TBS transition parameter is almost constant ($N_{trans} \sim 6$) for droplets of $R > 6$ μm, and rises abruptly for smaller droplets (Fig. 7*B*). This behavior is in good agreement with previous studies of Xu and Crooker (34), which focused on a static analysis. This striking similarity indicates that PSS droplets behave identically to equilibrium structures, as expected from the previous demonstration of a photoisomerization process being slower than the liquid crystal film equilibrium (43). On the other hand, the agreement with the work of Xu and Crooker occurs despite the use of a different LC matrix (E7 vs. ZLI-4788-000). This suggests that the N_{trans} variation with *R* depends only slightly on the precise elastic constants, or on the anchoring strength values. In addition, we have been able to consider for each value of cholesteric pitch (both IS and PSS) the *b*TBS structure, defined by the angle associated with the position of the two defects, intermediate between TBS ($\Theta = 180°$) and RSS ($\Theta < 60°$). The continuous evolution of Θ, observed in *b*TBS for IS and PSS droplets (Fig. 8) is in good agreement with recently reported combined experimental and simulated data on cholesteric droplets (35). The fact that this evolution occurs for different *N*, depending on the pitch value, is directly correlated to the variation of N_{trans} with *R* (Fig. 7*B*).

The observation of the increasing N_{trans} values when *R* decreases highlights the strong influence of confinement in cholesteric droplets, which is also revealed by the trend of stronger elongation of *p* (in comparison with the intrinsic cholesteric pitch) for decreasing *N* (Fig. 2*A*). Since the elastic constants are quite close for all of the liquid crystals here considered, E7 (44, 45), ZLI for Xu and Crooker work (46, 47), and 5CB for the simulations (48), we can understand the very similar $N_{trans}(R)$ evolution observed for E7 and ZLI. It, however, also suggests that the anchoring strength (which may be different for the different liquid crystals) does not play a crucial role in these features, a finding that is confirmed by the results of simulations (Fig. S3). It is shown in Fig. 3*A* that a high curvature, in particular leads to large splay values close to the center of CLC droplet. As a result, the *p* variation with *R* is recovered in simulations. Particularly large features are observed for small droplets; we could therefore infer that the influence of a large curvature might be even higher than that one calculated using a Landau–de Gennes model under a one-constant approximation. Note that the three liquid crystals used here all have K33 > K11 > K22. In future work, we plan to consider this inequality to better describe the evolution of N_{trans} with *R*.
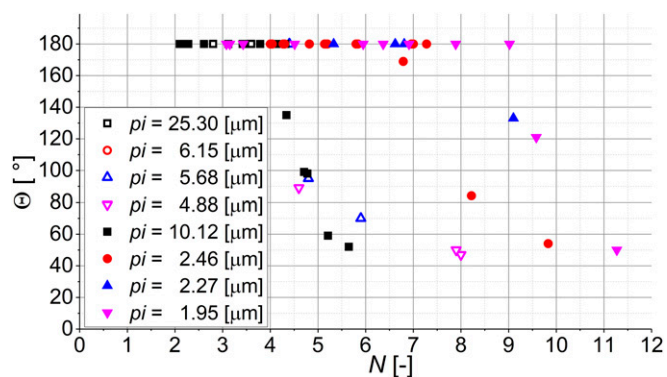

Fig. 8. Probing of the appearance of the intermediate bent structure, defined by a texture with two nondiametrically oriented boojums. Dependence of Θ on *N*, for droplets in IS and PSS (full and hollow symbols, respectively).

Conclusions

We have shown that the change of the cholesteric pitch driven by UV irradiation in the presence of an overcrowded alkene-based unidirectional molecular motor provides an effective means to not only control the symmetry of cholesteric droplet by controlling positions of topological defects dynamically, but also to control the RSS handedness. The latter was possible due to a large amplitude of initial and PSS values of HTP of motor in E7, which we believe is a particularly important parameter for the study of (photo)dynamic response of CLC droplets.

We have demonstrated the inverse of handedness by the reappearance of an RSS texture, and by the change of the orientation of the *b*TBS state. Simulations of the CLC droplet structures allowed us to identify the dynamical states spanning from TBS, *b*TBS, and RSS under irradiation, and served to underline that the influence of the confinement parameters on the optical signature is invariant, regardless of whether static or dynamic equilibrium is established. When combined with our experimental results, our findings reveal a particularly strong influence of confinement on droplets of liquid crystals with planar boundary conditions, likely in relation with the large distortion induced close to the droplet center, which may develop even further in droplets having a small radius.

Experimental

CLCs were prepared by doping of the E7 liquid crystal with enantiomerically pure molecular motor dopant. CLC droplets were fabricated by dispersing the liquid crystals in a glycerol matrix, and mechanical shearing after transferring on the microscope glass slide. The images were captured with the use of a polarized light microscope, either before or during the irradiation with a UV pencil lamp. For details, please see *Supporting Information*.

1. Lagerwall JPF, Scalia GA (2012) A new era for liquid crystal research: Applications of liquid crystals in soft matter nano-, bio- and microtechnology. *Curr Appl Phys* 12:1387–1412.
2. Palffy-Muhoray P, Cao W, Moreira M, Taheri B, Muñoz A (2006) Photonics and lasing in liquid crystal materials. *Philos Trans A Math Phys Eng Sci* 364:2747–2761.
3. Coles H, Morris S (2010) Liquid-crystal lasers. *Nat Photonics* 4:676–685.
4. Miller DS, Carlton RJ, Mushenheim PC, Abbott NL (2013) Introduction to optical methods for characterizing liquid crystals at interfaces. *Langmuir* 29:3154–3169.
5. Muševič I (2014) Integrated and topological liquid crystal photonics. *Liq Cryst* 41:418–429.
6. Lopez-Leon T, Fernandez-Nieves A (2011) Drops and shells of liquid crystal. *Colloid Polym Sci* 289:345–359.
7. Darmon A, Benzaquen M, Čopar S, Dauchot O, Lopez-Leon T (2016) Topological defects in cholesteric liquid crystal shells. *Soft Matter* 12:9280–9288.
8. Lavrentovich OD (1998) Topological defects in dispersed liquid crystals, or words and worlds around liquid crystals, or liquid crystal drops. *Liq Cryst* 24:117–126.
9. Muševič I, Škarabot M, Humar M (2011) Direct and inverted nematic dispersions for soft matter photonics. *J Phys Condens Matter* 23:284112.
10. Humar M, Ravnik M, Pajk S, Muševič I (2009) Electrically tunable liquid crystal optical microresonators. *Nat Photonics* 3:595–600.
11. Tomar V, Hernandez SI, Abbott NL, Hernandez-Ortiz JP, de Pablo JJ (2012) Morphological transitions in liquid crystal nanodroplets. *Soft Matter* 8:8679–8689.
12. Humar M, Muševič I (2010) 3D microlasers from self-assembled cholesteric liquid-crystal microdroplets. *Opt Express* 18:26995–27003.
13. Moreira MF, et al. (2004) Cholesteric liquid-crystal laser as an optic fiber-based temperature sensor. *Appl Phys Lett* 85:2691–2693.
14. Humar M, Muševič I (2011) Surfactant sensing based on whispering-gallery-mode lasing in liquid-crystal microdroplets. *Opt Express* 19:19836–19844.
15. Lin IH, et al. (2011) Endotoxin-induced structural transformations in liquid crystalline droplets. *Science* 332:1297–1300.
16. Carlton RJ, et al. (2013) Chemical and biological sensing using liquid crystals. *Liq Cryst Rev* 1:29–51.
17. Noh J, Liang HL, Drevensek-Olenik I, Lagerwall JPF (2014) Tuneable multicoloured patterns from photonic cross-communication between cholesteric liquid crystal droplets. *J Mater Chem C* 2:806–810.
18. Fan J, et al. (2015) Light-directing omnidirectional circularly polarized reflection from liquid-crystal droplets. *Angew Chem Int Ed Engl* 54:2160–2164.
19. Aβhoff SJ, et al. (2015) Superstructures of chiral nematic microspheres as all-optical switchable distributors of light. *Sci Rep* 5:14183.
20. Lin JD, et al. (2013) Optically tunable/switchable omnidirectionally spherical microlaser based on a dye-doped cholesteric liquid crystal microdroplet with an azo-chiral dopant. *Opt Express* 21:15765–15776.
21. Wang L, et al. (2015) Luminescence-driven reversible handedness inversion of self-organized helical superstructures enabled by a novel near-infrared light nanotransducer. *Adv Mater* 27:2065–2069.
22. Wang Y, Li Q (2012) Light-driven chiral molecular switches or motors in liquid crystals. *Adv Mater* 24:1926–1945.
23. Zheng ZG, et al. (2015) Wide tunable lasing in photoresponsive chiral liquid crystal emulsion. *J Mater Chem C* 3:2462–2470.
24. Li Y, Wang M, White TJ, Bunning TJ, Li Q (2013) Azoarenes with opposite chiral configurations: light-driven reversible handedness inversion in self-organized helical superstructures. *Angew Chem Int Ed Engl* 52:8925–8929.
25. Li Y, Xue C, Wang M, Urbas A, Li Q (2013) Photodynamic chiral molecular switches with thermal stability: from reflection wavelength tuning to handedness inversion of self-organized helical superstructures. *Angew Chem Int Ed Engl* 52:13703–13707.
26. Asshoff SJ, et al. (2013) Time-programmed helix inversion in phototunable liquid crystals. *Chem Commun (Camb)* 49:4256–4258.
27. Katsonis N, Lacaze E, Ferrarini A (2012) Controlling chirality with helix inversion in cholesteric liquid crystals. *J Mater Chem* 22:7088–7097.
28. Eelkema R, Feringa BL (2006) Amplification of chirality in liquid crystals. *Org Biomol Chem* 4:3729–3745.
29. Eelkema R, et al. (2006) Rotational reorganization of doped cholesteric liquid crystalline films. *J Am Chem Soc* 128:14397–14407.
30. Bezic J, Žumer S (1992) Structures of the cholesteric liquid crystal droplets with parallel surface anchoring. *Liq Cryst* 11:593–619.
31. Bajc J, Bezic J, Žumer S (1995) Chiral nematic droplets with tangential anchoring and negative dielectric anisotropy in an electric field. *Phys Rev E Stat Phys Plasmas Fluids Relat Interdiscip Topics* 51:2176–2189.
32. Seč D, Porenta T, Ravnik M, Žumer S (2012) Chiral nematic droplets with tangential anchoring and negative dielectric anisotropy in an electric field. *Soft Matter* 8:11982–11988.
33. Kurik MV, Lavrentovich OD (1982) Negative-positive monopole transitions in cholesteric liquid crystals. *JETP Lett* 35:444–447.
34. Xu F, Crooker PP (1997) Chiral nematic droplets with parallel surface anchoring. *Phys Rev E* 56:6853–6860.
35. Zhou Y, et al. (2016) Structural transitions in cholesteric liquid crystal droplets. *ACS Nano* 10:6484–6490.
36. Lee G, et al. (2013) Photoinduced ordering transition in microdroplets of liquid crystals with azo-dendrimer. *Part Part Syst Charact* 30:847–852.
37. Orlova T, Aβhoff SJ, Yamaguchi T, Katsonis N, Brasselet E (2015) Creation and manipulation of topological states in chiral nematic microspheres. *Nat Commun* 6:7603.
38. Gvozdovskyy I, Yaroshchuk O, Serbina M, Yamaguchi R (2012) Photoinduced helical inversion in cholesteric liquid crystal cells with homeotropic anchoring. *Opt Express* 20:3499–3508.
39. Chen J, et al. (2014) Textures of cholesteric droplets controlled by photo-switching chirality at the molecular level. *J Mater Chem C* 2:8137–8141.
40. Wang L, et al. (2017) Optically reconfigurable chiral microspheres of self-organized helical superstructures with handedness inversion. *Mater Horiz* 4:1190–1195.
41. Orlova T, et al. (February 12, 2018) Revolving supramolecular chiral structures powered by light in nanomotor-doped liquid crystals. *Nat Nanotech*, 10.1038/s41565-017-0059-x.
42. Bukusoglu E, et al. (2016) Positioning colloids at the surfaces of cholesteric liquid crystal droplets. *Soft Matter* 12:8781–8789.
43. Bosco A, et al. (2008) Photoinduced reorganization of motor-doped chiral liquid crystals: bridging molecular isomerization and texture rotation. *J Am Chem Soc* 130:14615–14624.
44. Klus B, Laudyn UA, Karpierz MA, Sahraoui B (2014) All-optical measurement of elastic constants in nematic liquid crystals. *Opt Express* 22:30257–30266.
45. Hakemi H, Jagodzinski EF, Dupré DB (1983) Temperature dependence of the anisotropy of turbidity and elastic constants of nematic liquid crystal mixture E7. *Mol Cryst Liq Cryst* 91:129–136.
46. Podoliak N, et al. (2014) Elastic constants, viscosity and response time in nematic liquid crystals doped with ferroelectric nanoparticles. *RSC Adv* 4:46068–46074.
47. Koyama K, Kawaida M, Akahane T (1989) A method for determination of elastic constants K_1, K_2, K_3 of a nematic liquid crystal only using a homogeneously aligned cell. *Jpn J Appl Phys* 28:1412–1416.
48. Bradshaw MJ, Raynes EP, Bunning JD, Faber TE (1985) The Frank constants of some nematic liquid crystals. *J Phys France* 46:1513–1520.